Signatures of quantum transport through two-dimensional structures with correlated and anticorrelated interfaces

Tony Low[1] and Davood Ansari[2]
[1]*Department of Electrical and Computer Engineering, Purdue University, West Lafayette, Indiana 47906, USA*
[2]*Department of Electrical and Computer Engineering, National University of Singapore, Singapore 119077, Singapore*
(Received 9 June 2008; revised manuscript received 3 September 2008; published 1 October 2008)

Electronic transport through a two-dimensional decananometer length channel with correlated and anticorrelated surfaces morphologies is studied using the Keldysh nonequilibrium Green's-function technique. Due to the pseudoperiodicity of these structures, the energy-resolved transmission possesses pseudoband and pseudogap. Channels with correlated surfaces are found to exhibit wider pseudobands than their anticorrelated counterparts. By surveying channels with various combinations of material parameters, we found that a smaller transport mass increases the channel transmittivity and energy bandwidth of the pseudobands. A larger quantization mass yields a larger transmittivity in channels with anticorrelated surfaces. For channels with correlated surfaces, the dependence of transmittivity on quantization mass is complicated by odd-to-even mode transitions. An enhanced threshold energy in the energy-resolved transmission can also be observed in the presence of surface roughness. The computed enhanced threshold energy was able to achieve agreement with the experimental data for Si⟨110⟩ and Si⟨100⟩ devices.

DOI: 10.1103/PhysRevB.78.165301 PACS number(s): 73.50.−h, 72.20.Dp, 73.21.Fg, 73.23.Ad

I. INTRODUCTION

In the literature, theoretical studies of the physics of surface roughness on electronic transport properties mainly focus on the linear response near thermodynamic equilibrium. In this regime, transport is diffusive and the electron dynamics is well described by a Boltzmann equation[1] or Kubo formula.[2] Once the perturbation Hamiltonian for surface roughness (H_{SR}) is formulated, the transition amplitude between electronic states can be computed through Fermi's golden rule. Surface roughness limited mobility can then be systematically calculated. The theory on the form of H_{SR} traces back to the work by Prange and Nee[3] on magnetic surface states in metals. More recently, a systematic derivation of H_{SR} was discussed by Ando[4] in the context of electronic transport in semiconductors.

It is well understood that this perturbation Hamiltonian consists of two parts:[5] (i) local energy-level fluctuations and (ii) local charge-density fluctuations. The first term (i.e., local energy-level fluctuations) is usually introduced phenomenologically[6] and explains the experimental observation that the surface roughness limited electron mobility in a quantum well scales with the film thickness (T_b) and with the material quantization mass (m_z) according to T_b^{-6} and m_z^2, respectively.[6–9] The latter term (i.e., local charge-density fluctuations) is believed to be an important contribution to the degradation of electron mobility in the high inversion charge-density regime.[10] Although the treatment of the surface roughness problem is usually conducted in the framework of effective-mass theory, a microscopic and self-consistent determination of H_{SR} can be obtained through density-functional theory.[11] Another manifestation of surface roughness in quantum wells is the enhanced threshold energy, which has recently been observed experimentally[7] in quantum wells with thickness <4 nm. These experiments show that the observed threshold energy does not follow the expected inverse quadratic scaling relationship with T_b. An objective of this paper is to explain why this deviation from quadratic scaling occurs.

The physical effects of surface roughness on phase-coherent transport become very convoluted when the quantum well surfaces are roughened with random inhomogenuity of different scales.[12] We limit our study to phase-coherent electronic transport through quantum wells with two special kinds of surface roughness morphology: (i) perfectly correlated surface roughness and (ii) perfectly anticorrelated surface roughness morphologies. Phase-coherent transport could be possible as devices are scaled into the decananometer regimes.[13] In practice, one would expect a quantum well grown using the atomic layer deposition technique to produce a high degree of correlation between the two surfaces. Studies of surface roughness scattering in the diffusive regime usually ignore such surface correlation effects.[5] Herein, we show that phase-coherent transport through quantum wells with perfectly correlated or perfectly anticorrelated surfaces gives rise to distinctive features in the energy-resolved transmission profile. The theoretical method we had employed is the Keldysh nonequilirium Green's-function (NEGF) approach[14–17] within a finite element and boundary element discretization scheme.[18–20]

This paper is organized as follows. Section II discusses the NEGF formalism and methodology in a finite element discretization scheme. Section III examines the energy-resolved transmission characteristics for quantum films with correlated and anticorrelated surfaces. We discuss these results in comparison to the Kronig-Penny model.[21] Section IV studies the impact of quantization and transport masses on the transmission characteristics. Finally, we compare our results to experimental values of the enhanced threshold energy for Si⟨100⟩ and Si⟨110⟩ devices.

II. THEORY AND MODEL

The Landauer approach[22,23] pictures a device within which dissipative processes are absent but coupled to perfect

 ©2008 The American Physical Society

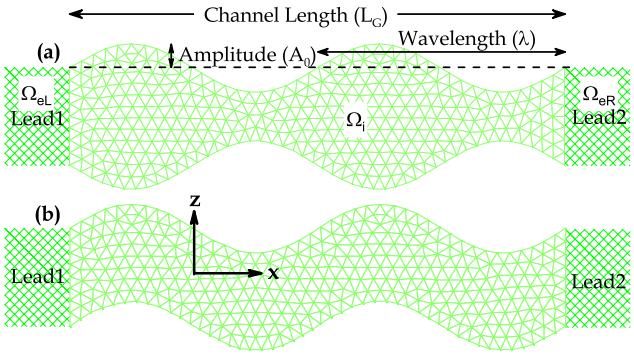

FIG. 1. (Color online) Illustration of the mesh used for simulation of 10 nm 2D channel with (a) anticorrelated and (b) perfectly correlated surfaces. In our work, the roughness is characterized by only two parameters: amplitude (A_0) and wavelength (λ) as depicted in (a). The meshes are generated with an average distance of 0.25 nm.

thermodynamic systems known as "contacts." This approach has been very successful in modeling physical effects in myriad of problems in the field of mesoscopic physics.[24] When irreversible or energy dissipating processes are present in the device, a more sophisticated quantum transport model such as the NEGF is needed to account for the coupling and transitions between the different quantum states in the system. The NEGF method was first formulated by Kadanoff and Baym[25] and Keldysh.[15] Discussions of NEGF and its applications to condensed-matter phenomena can be found in textbooks by Datta,[14] Haug,[16] and Mahan.[17]

This section summarizes the NEGF formalism applied to electronic transport through a two-dimensional (2D) channel implemented using the finite element (FEM) and boundary element (BEM) discretization scheme.[18] Our choice of FEM over finite difference method is mainly because it can resolve the device's roughened surface geometry more efficiently with its flexible mesh. Our methods are similar to the ones developed by Havu *et al.*[20,26] and Polizzi and Datta.[19]

Figure 1 illustrates 2D channels with correlated and anticorrelated surface morphologies. The problem domain is denoted by Ω, with points represented by a 2D spatial coordinate $r=(x,z)\in\Omega$. Ω is then partition into the interior Ω_i and exterior domains Ω_{ej}, where $j=L,R,0$. Ω_{eL} and Ω_{eR} denote the left and right leads, respectively, while Ω_{e0} denotes the remaining space. Each exterior domain Ω_{ej} shares the boundary with Ω_i denoted as $\partial\Omega_{ij}$. The boundary of Ω_i is simply $\partial\Omega_i=\Sigma_j\partial\Omega_{ij}$. The goal is to seek the numerical solution of the Green's function in Ω_i denoted by $G(r,r')$. In our problem, the exterior domains Ω_{ej} consists of semi-infinite leads with known Green's functions.[14] Therefore, BEM can be applied to each of these exterior domain to account for its effect on the respective boundaries Ω_{ij}. The purpose of FEM is to formulate the differential equation within Ω_i.

Within the effective-mass approximation, the 2D Hamiltonian that we are solving can be written as

$$\hat{H}\Psi(r)\equiv-\frac{\hbar^2}{2}\nabla_r\cdot[\bar{M}(r)\nabla_r\Psi(r)]+V(r)\Psi(r)=\epsilon\Psi(r), \quad (1)$$

where $r=(x,z)\in\Omega$ and $\bar{M}(r)$ is a 2×2 effective-mass tensor. In this work, we assumed an effective-mass tensor with the following matrix elements: $[\bar{M}]_{11}=m_x^{-1}$, $[\bar{M}]_{12}=0$, $[\bar{M}]_{21}=0$, and $[\bar{M}]_{22}=m_z^{-1}$. m_x and m_z are the transport and quantization masses, respectively. The Green's function of $\hat{H}$ is defined as

$$[\epsilon+i\eta-\hat{H}]G(r,r')=\delta(r-r'):r\in\Omega, \quad (2)$$

where the boundary condition of outgoing waves is incorporated by the introduction of $\eta\to0^+$; i.e., $G(r,r')$ is the retarded Green's function. $\delta(r-r')$ is the Dirac delta function. In the FEM scheme, we have the node-wise shape functions $\alpha_i(r)$ as our basis functions;[18] i.e., linear basis functions are employed in this work. Using the properties of a Dirac delta function of Eq. (2), we can write α_h as follows:

$$\alpha_h(r')=\int_{r\in\Omega_i}\alpha_h(r)[-V(r)+\epsilon+i\eta]G(r,r')d\Omega + \int_{r\in\Omega_i}\alpha_h(r)\frac{\hbar^2}{2}\nabla_r\cdot[\bar{M}(r)\nabla_rG(r,r')]d\Omega:r'\in\Omega_i. \quad (3)$$

The second integral term on the right-hand side of Eq. (3) contains a second-order differential integrand. It can be reduced to first order via the identity,

$$f_1\nabla\cdot[f_2\nabla f_3]=\nabla\cdot[f_1f_2\nabla f_3]-f_2\nabla f_1\cdot\nabla f_3. \quad (4)$$

Equation (3) then becomes

$$\alpha_h(r')=\int_{r\in\Omega_i}\alpha_h(r)[-V(r)+\epsilon+i\eta]G(r,r')d\Omega + \int_{r\in\partial\Omega_i}\left[\alpha_h(r)\frac{\hbar^2}{2}\bar{M}(r)\nabla_rG(r,r')\right]\cdot\hat{n}d\partial\Omega_i - \int_{r\in\Omega_i}\bar{M}(r)\nabla_r\alpha_h(r)\frac{\hbar^2}{2}\cdot\nabla_rG(r,r')d\Omega:r'\in\Omega_i, \quad (5)$$

where $\hat{n}$ in Eq. (5) is the normal vector to the boundary $\partial\Omega_i$. We note that in order to obtain $\nabla_rG(r,r')$ along the boundary $\partial\Omega_i$, one requires information about the Green's function outside and within Ω_i. Recall that the Green's function of the exterior domain Ω_{ek} and G_{ek} has a simple analytical form.[14] For our purpose, we only need to know the explicit form of G_{ek} along the boundary $r_{ek}\in\partial\Omega_{ik}$,

$$G_{ek}(x_{ek},z_{ek};x_{ek},z'_{ek})=-\sum_{m=1}^{\infty}\chi_m(z_{ek})\chi_m(z'_{ek}) \times\frac{2\sin(\omega_mx_{ek})\exp(i\omega_mx_{ek})}{\hbar v_m}, \quad (6)$$

where v_m is the carrier velocity defined as $v_m=\hbar\omega_m/m_x$ and $\omega_m=(1/\hbar)\sqrt{2m_x(\epsilon-\kappa_m)}$. χ_m are the eigenstates of the confined modes in the leads corresponding to the eigenstate with energy κ_m. In order to incorporate the information of the exterior Green's function into Eq. (5), we express the term $\nabla_rG(r,r')$ in the last integral expression as[20]

$$\nabla_r G(r,r') = \int_{r_{ej}\in\partial\Omega_{ij}} G(r_{ej},r')\frac{\hbar^2}{2}\bar{M}(r_{ej})\nabla_r\nabla_{r_{ej}}G_{ej}(r_{ej},r) \times d\,\partial\Omega_{ej}: r \in \Omega_{ej}. \quad (7)$$

With this replacement to Eq. (5), the calculus part of the problem is complete and we are ready to formulate the problem in matrix form.

If we assume that the Green's function can be expressed in terms of the FEM basis as follows:

$$G(r,r') \approx \sum_{ij} \alpha_i(r)\alpha_j(r')G_{ij}, \quad (8)$$

then Eq. (5) can be formulated into a compact matrix equation by multiplying both sides by $\alpha_g(r')$ and integrating over r'. The matrix equation is

$$S = [\epsilon S - H - \Sigma]GS, \quad (9)$$

where $[S]_{gh} = \int \alpha_g(r')\alpha_h(r')dr'$ is commonly known as the overlap matrix. The explicit form for computing the matrix elements of Σ and H are given in Eq. (10),

$$[H]_{hi} \equiv \left\{ \int_{r\in\Omega_i} \alpha_h(r)[-V(r) + i\eta]\alpha_i(r) - \frac{\hbar^2}{2}\bar{M}(r)\nabla_r\alpha_h(r)\cdot\nabla_r\alpha_i(r)d\Omega \right\},$$

$$(\Sigma_k)_{hi} \equiv \left\{ \int_{r\in\partial\Omega_{ik}} \left[\alpha_h(r)\frac{\hbar^2}{2} \times \bar{M}(r) \int_{r_{ek}\in\partial\Omega_{ik}} \alpha_i(r_{ek})\frac{\hbar^2}{2}\bar{M}(r_{ek})\nabla_r\nabla_{r_{ek}} \times G_{ek}(r_{ek},r)d\,\partial\Omega_{ek} \right] \cdot \hat{n}d\,\partial\Omega_i \right\}. \quad (10)$$

With all these quantities known, we are ready to compute the device observables through the Green's function,

$$G(\epsilon) = [\epsilon S - H - \Sigma]^{-1}. \quad (11)$$

The device's local density of states is computed through the spectral function defined as

$$A(\epsilon) = G(\epsilon)^\dagger[\Gamma_L(\epsilon) + \Gamma_R(\epsilon)]G(\epsilon), \quad (12)$$

where $\Gamma = i[\Sigma - \Sigma^\dagger]$ are the broadening functions to be computed individually for each leads.[14] The diagonal elements of $A(\epsilon)$ yield the local density of states. Finally, the transmission is computed by taking the trace of the transmission function Φ defined to be[14]

$$\Phi(\epsilon) = \Gamma_L(\epsilon)G(\epsilon)\Gamma_R(\epsilon)G(\epsilon)^\dagger. \quad (13)$$

To facilitate our subsequent analysis, we unclustered the total transmission Φ and examine only the transmission characteristics between mode $m=1,2$ of left lead to mode $n=1,2$ of right lead. This mode-to-mode transmission (Φ_{mn}) is easily accomplished in our numerical scheme by noting that the lead self-energy can be unfolded into their respective modes,

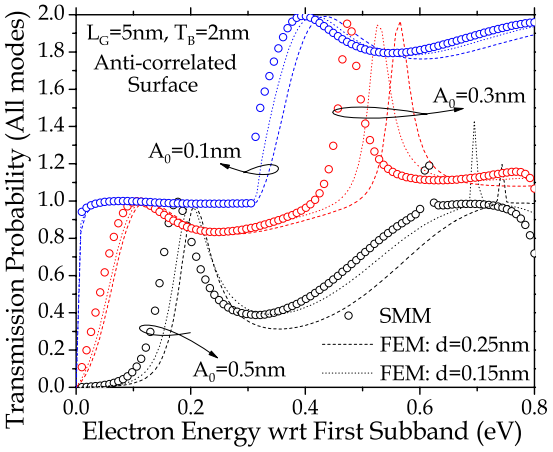

FIG. 2. (Color online) FEM and scattering matrix method (SMM) simulations of $L_G=5$ nm and $T_B=2$ nm channels with anticorrelated surfaces having roughness amplitudes $A_0=0.1,0.3,0.5$ nm and wavelength $\lambda=2.5$ nm. We assumed a transport mass $m_x=0.2m_0$ and a quantization mass $m_z=0.9m_0$, i.e., based on Si material. SMM is a "mode space" approach, which the quantized energy is resolved analytically.

$$G_{ek} = G_{ek}^1 + G_{ek}^2 + G_{ek}^3 \ldots, \quad (14)$$

where G_{ek}^m is the self-energy for mode m. This allows one to define a broadening function associated with each mode $\Gamma_{L/R}^{m/n}$ from which the respective mode-to-mode transmission Φ_{mn} can be computed. With this understanding, we shall begin our numerical analysis.

Figure 1 illustrates a typical FEM mesh with [Fig. 1(a)] anticorrelated and [Fig. 1(b)] perfectly correlated surfaces used in our calculations. The FEM mesh is generated using the algorithm developed by Persson and Strang[27] based on the well-known Delaunay triangulation routine. In our work, the roughness is characterized by sinusoidal profiles with only two parameters: amplitude (A_0) and wavelength (λ). These parameters are analogous to the root-mean-square roughness and the roughness autocorrelation length commonly employed in the literatures to describe the surface morphology.[28] In Fig. 2, we compare the energy-resolved transmission calculated with our FEM-BEM method to the SMM (Ref. 29) using various mesh sizes d. In the SMM approach, the quantized energies are resolved analytically unlike the FEM-BEM or finite difference approaches. The simulations used a channel length $L_G=5$ nm, an average film thickness $T_B=2$ nm, a transport mass $m_x=0.2m_0$, and a quantization mass $m_z=0.9m_0$. Anticorrelated surfaces described by roughness amplitudes $A_0=0.1,0.3,0.5$ nm and wavelength $\lambda=2.5$ nm were considered. As shown in Fig. 2, the FEM-BEM results are in satisfactory agreement with SMM. A very fine spatial discretization in the transport direction was employed for the SMM calculations.

III. GENERAL FEATURES IN ENERGY-RESOLVED TRANSMISSION

The objective of this section is to perform a systematic analysis of the transmission characteristics of electronic

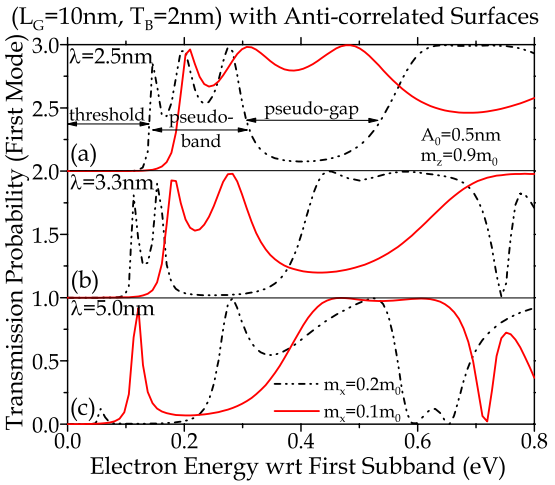

FIG. 3. (Color online) Energy-resolved transmission (for Φ_{11}) from FEM simulation of $L_G=10$ nm and $T_B=2$ nm channels with various anticorrelated surfaces with roughness amplitude $A_0=0.5$ nm and wavelengths (a) $\lambda=2.5$, (b) 3.3, and (c) 5.0 nm. For each structure, we simulated transport masses of $m_x=0.2m_0$ (dash-dotted lines) and $m_x=0.1m_0$ (solid lines) each with quantization mass $m_z=0.9m_0$.

transport through a 2D quantum channel with correlated and anticorrelated surfaces. As a model system, we adopted a set of parameter values typical of "end-of-road-map" devices,[30] i.e., a $L_G=10$ nm 2D channel with an average quantum film thickness of $T_B=2$ nm. For each class of devices, the effects of material properties and the degree of roughness on the energy-resolved transmission characteristics were examined. The material band structure was parametrized by a set of effective masses, i.e., transport mass m_x and quantization mass m_z. Although microscopic details of the atomic structure of interfaces[11] and related elemental defects (i.e., Si-Si and Si-O-Si bonds)[21] could be a source of interface scattering, it is not the main focus of this work. Ignoring these interfacial elemental defects, we study the geometrical effect of surface roughness on the transport characteristics.

A. Transmission through anticorrelated surfaces

Figure 3 shows the energy-resolved transmission characteristics $\Phi_{mn=11}$ (first mode to first mode transmission) for devices with anticorrelated surfaces. Three different sets of roughness parameters were simulated: [Fig. 3(a)] $A_0=0.5$ nm and $\lambda=2.5$ nm, [Fig. 3(b)] $A_0=0.5$ nm and $\lambda=3.3$ nm, and [Fig. 3(c)] $A_0=0.5$ nm and $\lambda=5.0$ nm. For each set of roughness parameters, the following sets of material parameters were simulated: (dash-dotted lines) $m_z=0.9m_0$ with $m_x=0.2m_0$ and (solid lines) $m_z=0.9m_0$ with $m_x=0.1m_0$.

Several general observations can be made about the energy-resolved transmission spectra: (i) there are regions of pseudogaps and pseudobands where transmittivity is relatively opaque and transparent, respectively; (ii) within the pseudobands, there are camel-back structures which increase in number with increasing roughness frequency (i.e., decreasing λ); and (iii) a delayed "turn on" of transmission called "enhanced threshold," which increases with increasing roughness frequency. The enhanced threshold energy is a geometrically derived property due to 2D quantization effects of the roughened morphology. The enhanced threshold is zero for an unroughened quantum well channel. Note that the energy scale is referenced from the subband energy of the first mode in the lead previously defined as κ_1. In addition, due to the symmetry of the problem, $\Phi_{mn}\neq 0$ if and only if both m and n are odd/even numbers.

Due to the anticorrelated surface morphology, the thickness of the 2D quantum film fluctuates from the source to drain contacts. Henceforth, we can visualize the electron as moving across the channel through an undulating energy landscape caused by the variable film thickness. This accounts for the appearance of camel-back structures in the pseudoband region of the energy-resolved transmission as depicted in Fig. 3, i.e., a signature of resonant tunneling. The undulating energy landscape $[\epsilon_{\mathrm{QW}}(x)]$ can be modeled by a series of quantum wells (E_{QW}) as follows:

$$\epsilon_{\mathrm{QW}}(x)=\frac{\hbar^2\pi^2}{2m_z[T_B+2A_0\cos(2\pi x/\lambda)]^2}=\sum_j E_{\mathrm{QW}}(x+j\lambda). \tag{15}$$

E_{QW} can be expanded as a Taylor series to give the following leading-order terms:

$$E_{\mathrm{QW}}(x)\approx\left[\frac{\hbar^2\pi^2}{2m_z(T_B+2A_0)^2}+\frac{4\hbar^2\pi^4A_0x^2}{m_z(T_B+2A_0)^3\lambda^2}\right]U(x), \tag{16}$$

where $U(x)$ is a unit pulse at $-\lambda/2<x<\lambda/2$. The second term in Eq. (16) with the kinetic operator will yield the quantized energy levels of a harmonic oscillator with energies $\xi_n=\hbar\omega(n+0.5)$ where

$$\omega=\sqrt{\frac{8\hbar^2\pi^4A_0}{\lambda^2m_xm_z(T_B+2A_0)^3}}. \tag{17}$$

From the above expression, we have $\omega\propto m_x^{-0.5}$. Indeed, Fig. 3 reveals that a smaller m_x will yield a wider energy separation between the peaks of the camel-back structure. This also translates to a larger pseudoband bandwidth (BW). For the structure illustrated in Fig. 3, the estimated first quantized energy using Eq. (17) is $\xi_1\approx 0.1357$, 0.1019, and 0.0679 eV for $\lambda=2.5$, 3.33, and 5 nm, respectively. These estimates are in good agreement with threshold energies computed in Fig. 3, which is the energy needed for the first appearance of a transmission resonance.

To explain the global features of pseudobands and pseudogaps in the energy-resolved transmission results, we shall first review the pertinent results from the Kronig-Penny model.[31] Consider a periodically varying rectangular energy barrier as depicted in the inset of Fig. 4 with barrier energy of U_b and a spatial period of λ. The band structure (energy ξ versus momentum κ dispersion relation) of this one-dimensional (1D) periodic potential can be described by the following transcendental equation:

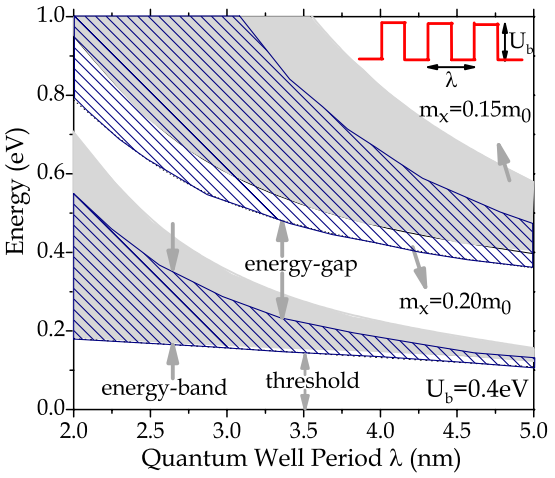

FIG. 4. (Color online) Available energy-band states (indicated by shaded regions) for a Kronig-Penny 1D crystal with periodically varying square potential wells plotted with respect to the quantum well width λ. The quantum well energy barrier U_b is set to be 0.4 eV. Effective masses of $m_x=0.15m_0$ (solid) and $m_x=0.2m_0$ (patterned) are considered.

$$\kappa = \pm \frac{1}{\lambda}\tan^{-1}\left(\frac{\sqrt{4-\alpha_i^2}}{\alpha}\right), \tag{18}$$

where α is given by

$$\alpha = 2\cosh\left(\frac{k_2\lambda}{2}\right)\cos\left(\frac{k_1\lambda}{2}\right) + \frac{k_2^2-k_1^2}{k_1k_2}\sinh\left(\frac{k_2\lambda}{2}\right)\sin\left(\frac{k_1\lambda}{2}\right), \tag{19}$$

when $0<\xi<U_b$ and

$$\alpha = 2\cos\left(\frac{k_2\lambda}{2}\right)\cos\left(\frac{k_1\lambda}{2}\right) - \frac{k_2^2+k_1^2}{k_1k_2}\sin\left(\frac{k_2\lambda}{2}\right)\sin\left(\frac{k_1\lambda}{2}\right), \tag{20}$$

when $\xi>U_b$. In addition, we have $\hbar k_1=\sqrt{2m_x|\xi|}$ and $\hbar k_2=\sqrt{2m_x|\xi-U_b|}$.

Figure 4 surveys the band structure of a Kronig-Penny 1D crystal under different quantum well periods λ where regions with propagating states are shaded. The analysis set is conducted for transport masses of $m_x=0.15m_0$ (colored region) and $m_x=0.2m_0$ (shaded region). The following observations can be made: (i) the energy bandwidth and threshold energy increase monotonically with decreasing quantum well period λ; (ii) energy bandwidth decreases monotonically with decreasing quantum well period λ; and (iii) a smaller transport mass m_x yields a larger energy bandwidth. Examination of the energy-resolved transmission in Fig. 3 shows that the pseudoband and enhanced threshold in the quasiperiodic 2D structure with anticorrelated surface roughness exhibit a strikingly similar trend with the Kronig-Penny model analysis. Based on these arguments, we conclude that the generic features of pseudoband and pseudogap observed in the energy-resolved transmission of the 2D film with anticorrelated surfaces are results of the film's quasiperiodicity.

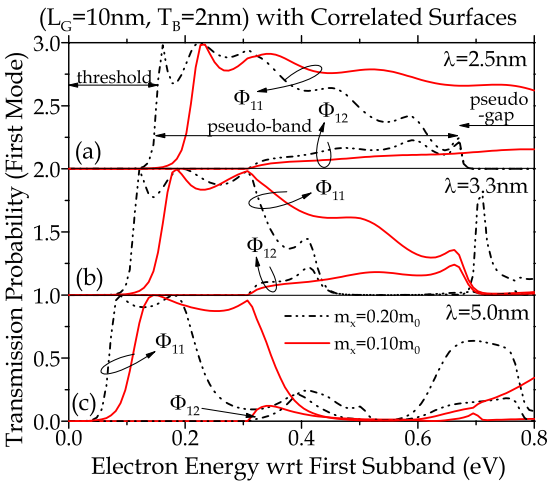

FIG. 5. (Color online) Energy-resolved transmission (for Φ_{11} and Φ_{12}) from FEM simulation of $L_G=10$ nm and $T_B=2$ nm channels with various perfectly correlated surfaces with roughness amplitudes $A_0=0.5$ nm and wavelengths (a) λ=2.5 nm, (b) λ=3.3 nm, and (c) λ=5.0 nm. For each structure, we simulated transport masses of $m_x=0.2m_0$ (dash-dotted lines) and $m_x=0.1m_0$ (solid lines) each with quantization mass $m_z=0.9m_0$.

B. Transmission through perfectly correlated surfaces

Figure 5 shows the energy-resolved transmission characteristic of a 2D channel with perfectly correlated surface roughness. The same sets of devices as performed in the anticorrelated case, with various surface roughness parameters and transport mass m_x, are simulated. Due to the different symmetry in this case, $\Phi_{mn}\neq 0$ for odd-to-even mode transition unlike the situation for anticorrelated surfaces. Therefore, we plotted the transmission characteristics Φ_{11} and Φ_{12} in Fig. 5, although we will mainly focus on Φ_{11} in the subsequent discussion.

As shown in Fig. 5, the generic features of pseudoband, pseudogap, and enhanced threshold induced by the quasiperiodicity are also present in structures with perfectly correlated surfaces. For each particular set of surface roughness parameters, the channel with perfectly correlated surfaces exhibits a distinctively larger pseudoband than its anticorrelated counterpart. Since there is no variation of quantum well thickness along the channel, the scattering in this case is purely a result of 2D geometrical and side-wall boundary effects. As a result, one would expect the carrier to feel a less undulating energy landscape in the perfectly correlated case. Effectively, this translates to a smaller U_b in the Kronig-Penny picture, which will then correspondingly yield a larger pseudoband's bandwidth.

Figures 6 and 7 are intensity plots for the local density of states $G^\dagger(\epsilon)\Gamma_L^1(\epsilon)G(\epsilon)$ due to injection of carriers from the source contact for the anticorrelated and correlated cases, respectively. Brighter regions indicate higher density of states. The carriers are injected from the first mode eigenstates of the source lead. The surface roughness morphologies are both characterized by $A_0=0.5$ nm and λ=2.5 nm. The energy-resolved transmission spectra are plotted on their left. The local density of states at each of the resonance

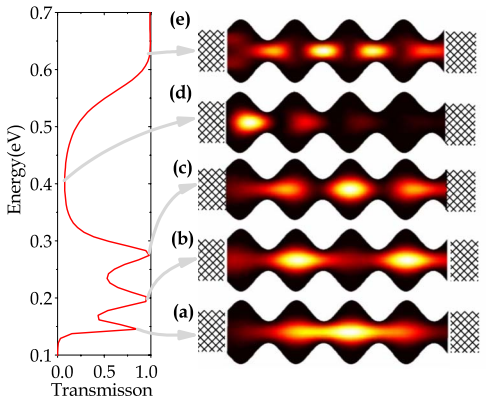

FIG. 6. (Color online) Intensity plot of local density of states due to the first mode of left contact, i.e., $G^{\dagger}\Gamma_L^1 G$, each at different injection energies (measured with respect to the lead's first quantized mode) as indicated. Device structure used are $L_G=10$ nm and $T_B=2$ nm channels with anticorrelated surfaces with roughness amplitude $A_0=0.5$ nm and wavelength $\lambda=2.5$ nm. A transport mass of $m_x=0.2m_0$ and quantization mass of $m_z=0.9m_0$ are used. The corresponding energy-resolved transmission characteristics are plotted on the left.

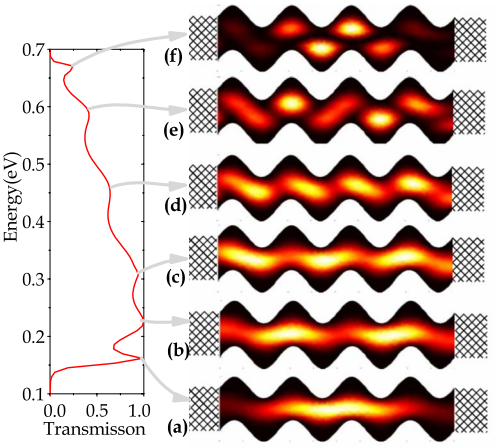

FIG. 7. (Color online) Similar to Fig. 6 except for a channel with perfectly correlated surfaces.

energies reveals localized high intensity patterns, which has its origin in interference effects due to multiple scattering of waves. One observes that the number of localized spots increases with the index of the resonance level. In the energy-resolved transmission, twice the number of resonance energy levels in the pseudoband is observed in the perfectly correlated case as compared to anticorrelated case. This is attributed to the reduced symmetry of the channel with a perfectly correlated surface morphology, which lacks the x-axis mirror symmetry of the anticorrelated surface. The degradation of the energy-resolved transmission at higher energy is due to the appearance of the second mode at 0.3 eV, which opens up a transmission through Φ_{12}. Therefore the resonance peak has a maximum transmission less than one.

IV. EFFECTIVE MASSES ON TRANSMITTIVITY AND THRESHOLD ENERGY

In this section, we study the impact of transport and quantization masses and surface roughness morphologies on the general characteristics of the energy-resolved transmission through a decananometer channel. Our analysis will be confined to the study of the first mode to first mode transmission Φ_{11}. We begin by proposing a reasonable metric for the measure of the transmittivity K of a channel,

$$K = \frac{1}{\mathrm{BW}} \int_{\mathrm{BW}} \Phi(\epsilon_{xz}) d\epsilon_{xz}, \tag{21}$$

where the pseudoband BW is defined as the energy difference between the last and first resonance peaks in the pseudoband. Enhanced threshold energy is defined as the energy for the appearance of the first resonance peak with respect to the lead's first subband energy, i.e., $\hbar^2\pi^2/(2m_z T_B^2)$. This phenomenon has been observed experimentally[7,9] and the suppression of its effect is pertinent to electronic device applications. Figure 8(c) provides an illustration of the concept of BW and enhanced threshold energy.

Figures 8(a), 8(b), 9(a), and 9(b) survey the BW and K for a decananometer channel of $\langle T_B \rangle = 2$ nm with anticorrelated and perfectly correlated surface roughness morphologies, respectively. Different sets of material parameters, i.e., $m_{x,z}$, are employed in the study. The key results can be summarized as follows: (i) a smaller m_x improves the BW and ef-

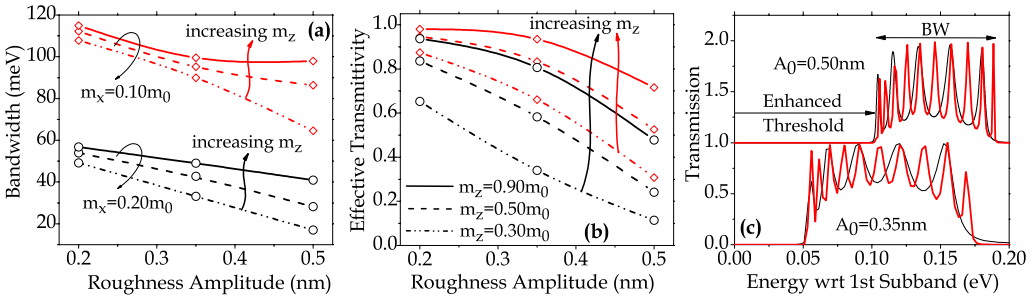

FIG. 8. (Color online) Surveying of pseudoband's bandwidth of the energy-resolved transmission for Φ_{11} [see Fig. 8(a)] and the transmittivity [see Fig. 8(b)] for various transport masses ($m_x=0.1m_0$ and $0.2m_0$ denoted by red and black lines, respectively) and quantization masses ($m_z=0.3m_0, 0.5m_0$ and $0.9m_0$ denoted by dash-dotted, dashed, and solid lines, respectively) plotted as functions of roughness amplitude A_0. Simulated for a device with $L_G=10$ nm and an average $T_B=2$ nm channel with anticorrelated surface roughness morphology ($\lambda=3.3$ nm). (c) Depicts the energy-resolved transmission for similar devices but with $L_G=20$ nm (black) and 40 mm (red) with various $A_0=0.35$ nm and 0.50 nm using effective masses of $m_x=0.2m_0$ and $m_z=0.9m_0$.

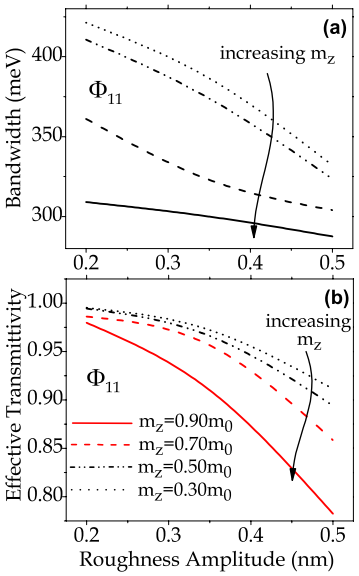

FIG. 9. (Color online) Effects of quantization mass (m_z) on the pseudoband's bandwidth of the energy-resolved transmission for Φ_{11} (a) and the transmittivity (b) through a channel with perfectly correlated surface roughness morphology plotted as a function of A_0. The device has $L_G=10$ nm and an average $T_B=2$ nm channel. Transport mass of $m_x=0.2m_0$ is used for all curves. The red curves in (b) denote that higher modes transitions, i.e., Φ_{12} and Φ_{22}, are present within the pseudobands of these structures.

fective transmittivity (K) for channels with anticorrelated and perfectly correlated surface roughness morphology and (ii) a larger m_z improves the transmittivity for channels with anticorrelated surface roughness but slightly degrades the transmittivity for channels with perfectly correlated surface roughness. The observation (i) is due to the increase in resonance linewidth as derived from the higher tunneling probability due to a smaller m_x.

In the diffusive regime, the surface roughness limited mobility for a quantum well scales proportionally with $\approx m_z^2\Delta^{-2}$, where Δ is the root-mean-square averaged fluctuation of the quantum well thickness.[8] In the channel with anticorrelated surfaces, $\Delta=\sqrt{2}A_0$. As depicted in Fig. 8(b), K increases with increasing m_z. For the channel with perfectly correlated surface morphology, Δ is zero. Thus, the main source of scattering mechanism in the "classical" sense is attributed to a local fluctuation of wave function.[5] In general, a larger m_z "propagates" the electron closer to the surfaces and renders it more sensitive to the surface roughness morphology. This explains the small degradation of K with increasing m_z. However, we must emphasize that the larger degradation of K [red curves in Fig. 9(b)] for $m_z=0.7m_0, 0.9m_0$ is due to the appearance of the second mode leading to a degradation of Φ_{11} while Φ_{12} begins to increase.

With a larger transmission bandwidth and relatively weak dependence of transmittivity on m_z, channel with highly correlated surfaces is more optimal for electronic transport in the phase-coherent regime. Especially for a channel with small quantization mass, i.e., III–V semiconductor alloys, the latter property is highly desirable for ballistic transport. Although these studies are conducted for a decananometer

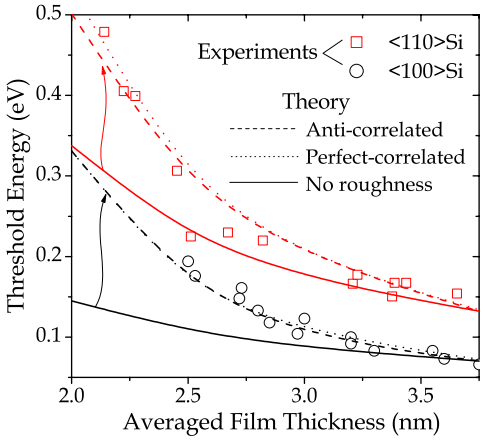

FIG. 10. (Color online) Theoretically calculated threshold energy as a function of the averaged 2D quantum film's thickness compared with the experimental data for Si⟨110⟩ (Ref. 9) and Si⟨100⟩ (Ref. 7) devices. For our calculations, a roughness amplitude of $A_0=0.5$ and 0.6 nm is able to describe the experimental data for Si⟨110⟩ and Si⟨100⟩ devices, respectively, where a roughness wavelength of $\lambda=2.5$ nm was assumed for both cases. The threshold energy for a channel with unroughened (solid lines), anticorrelated (dashed lines), and perfectly correlated (dotted lines) surfaces are plotted.

channel, we expect the results to be consistent for longer channel. To confirm this proposition, we considered the energy-resolved transmission for devices with $L_G=20$ and 40 nm in Fig. 8(c). The increase in channel length results in more resonance peaks (i.e., the number of peaks within the pseudoband is proportional to the number of sinusoidal cycles in the roughness morphology of the channel) but with the global features of enhanced threshold and the pseudoband's bandwidth intact. In particular, its energy-resolved transmission exhibits similar enveloping characteristics for different L_G, where the envelope is characteristic of a given A_0.

It has been reported that surface roughness will induce an additional threshold energy in quantum well devices and this effect had been systematically measured in experiments,[9,32] i.e., enhanced threshold energy. Therefore, the observed threshold energy will be greater than that described by the more commonly understood body quantization effect according to $\hbar^2\pi^2/(2m_zT_B^2)$. Figure 10 compares the theoretically calculated threshold energy of a roughened channel (i.e., perfectly correlated and anticorrelated surfaces morphology) with the available experimental data for Si⟨110⟩ and Si⟨100⟩ quantum well devices.[7,9] Assuming a roughness amplitude of $A_0=0.5$ and 0.6 nm for the Si⟨110⟩ and Si⟨100⟩ devices, respectively, we are able to match the experimental data for the range of quantum well thicknesses T_B. A roughness wavelength of $\lambda=2.5$ nm was assumed for all devices in our calculations. The corresponding threshold energy due to an unroughened channel is also shown (plotted as solid lines). A quantization mass (m_z) of $0.9m_0$ is employed for the Si⟨100⟩ devices. For Si⟨110⟩, the effective-mass tensor has off-diagonal terms in the direction normal to the quantum film surface. A unitary transformation is employed to decouple them as described by Stern and Howard.[33] Eventually, a

quantization mass of $0.33m_0$ is obtained for Si⟨110⟩ devices.

The enhanced threshold energy is a geometrically derived property of 2D quantization effects. The 2D geometry of the roughened channel introduces additional lateral confinement which serves to enhance overall threshold energy. Figures 6 and 7 illustrates this lateral confinement effect in channels with perfectly and anticorrelated surfaces. Note that these channels are constructed such that they retain the same volume as the unroughened channel. Equation (17) describes the approximate enhanced threshold energy due to surface roughness for the case of channels with anticorrelated surface morphology. Equation (17) tells us that the enhanced threshold energy is related to the material parameters according to $(m_x m_z)^{-1/2}$. Furthermore, contrary to the T_B^{-2} dependency in the usual case of body quantization, the enhanced threshold energy exhibits a $T_B^{-3/2}$ dependency as shown in Eq. (17). From the viewpoint of device performances, this translates to an additional threshold voltage shift. A small device threshold voltage shift is an important criterion to suppress the on-chip device-to-device electrical properties variations.[34]

V. CONCLUSION

The study of the impact of surface roughness on electronic transport usually focused on the dissipative regime with transport dynamics well governed by the classical Boltzmann's transport equation. Electronic transport through a channel with roughened surfaces in the phase-coherent regime is less understood. Using the Keldysh nonequilibrium Green's-function approach within a FEM-BEM numerical scheme, we performed a systematic study of quantum transport through a decananomater length quantum well channel with perfectly correlated and anticorrelated surfaces. Due to the pseudoperiodicity in these simulated structures, their energy-resolved transmission possesses pseudobands, pseudogaps, and an enhanced threshold energy. Channels with perfectly correlated surfaces exhibit wider pseudobands than their anticorrelated counterparts. Perfectly correlated channels also permit odd-to-even mode transition, which is not allowable in channel with anticorrelated surfaces.

An effective transmittivity in these structures is derived by computing the average transmission over the range of energy within the pseudoband. By surveying channels with various material parameters combinations (i.e., m_x and m_z), we found that a smaller transport mass m_x is beneficial for the transmittivity of the channel and serves to increase the energy bandwidth of the pseudoband. The observation of the contrasting trends in the dependence of transmittivity on m_z for anticorrelated and perfectly correlated surfaces is interesting. A quantum well with perfectly correlated surface is more optimal for channel material with smaller m_z. Technically speaking, a sufficiently correlated surface can be engineered via techniques like atomic layer deposition. Recall that the "classical" perturbing Hamiltonian due to surface roughness can be attributed to a local energy-level fluctuation and a local fluctuation of charge density.[5] On a general note, one could then say that channels with anticorrelated surfaces emphasize the former scattering mechanism, while the perfectly correlated surfaces emphasize the latter mechanism.

Lastly, we studied the phenomenon of enhanced threshold voltage shifts. Excellent corroboration with the experimental data was obtained. Enhanced threshold voltage shifts exhibit a $T_B^{-3/2}$ dependency, and its contribution to the total threshold energy is significant in the small T_B regime. Therefore, suppression of the device-to-device threshold voltage variations in quantum well channels with small quantization mass will present considerable challenge for the semiconductor device industry.[30]

ACKNOWLEDGMENTS

T.L. would like to thank M. S. Lundstrom for suggesting the examination of energy-resolved transmission for a longer channel and T. Manz for proofreading this manuscript. T.L. gratefully acknowledges the support of the Singapore Millennium Post-doctoral Foundation for the initial support of this work, also the Network for Computational Nanotechnology and the Nanoelectronics Research Initiative for their current support.

[1] M. V. Fischetti and S. E. Laux, Phys. Rev. B **48**, 2244 (1993).
[2] D. K. Ferry and S. M. Goodnick, *Transport in Nanostructures* (Cambridge University Press, Cambridge, England, 1999).
[3] R. E. Prange and T. W. Nee, Phys. Rev. **168**, 779 (1968).
[4] T. Ando, J. Phys. Soc. Jpn. **43**, 1616 (1977).
[5] C. Y. Mou and T. M. Hong, Phys. Rev. B **61**, 12612 (2000).
[6] H. Sakaki, T. Noda, K. Hirakawa, M. Tanaka, and T. Matsusue, Appl. Phys. Lett. **51**, 1934 (1987).
[7] K. Uchida, H. Watanabe, A. Kinoshita, J. Koga, T. Numata, and S. I. Takagi, Tech. Dig. - Int. Electron Devices Meet. **2002**, 47.
[8] T. Low, M. F. Li, C. Shen, Y. C. Yeo, Y. T. Hou, and C. Zhu, Appl. Phys. Lett. **85**, 2402 (2004).
[9] G. Tsutsui, M. Saitoh, and T. Hiramoto, IEEE Electron Device Lett. **26**, 836 (2005).
[10] S. Jin, M. V. Fischetti, and T. W. Tang, IEEE Trans. Electron Devices **54**, 2191 (2007).
[11] M. H. Evans, X. G. Zhang, J. D. Joannopoulos, and S. T. Pantelides, Phys. Rev. Lett. **95**, 106802 (2005).
[12] J. Wang, E. Polizzi, A. Ghosh, S. Datta, and M. Lundstrom, Appl. Phys. Lett. **87**, 043101 (2005).
[13] A. Schliemann, L. Worschech, A. Forchel, G. Curatola, and G. Iannaccone, Tech. Dig. - Int. Electron Devices Meet. **2004**, 1039.
[14] S. Datta, *Electronic Transport in Mesoscopic Systems* (Cambridge University Press, Cambridge, England, 1997).
[15] L. V. Keldysh, Zh. Eksp. Teor. Fiz. **47**, 1515 (1964).
[16] H. Haug and A. P. Jauho, Springer Series in Solid State Sciences (Springer, New York, 1996), p. 123.

[17] G. D. Mahan, *Many Particle Physics* (Plenum, New York, 1990).
[18] R. R. Mohan, *Finite Element and Boundary Element Applications in Quantum Mechanics* (Oxford University Press, New York, 2002).
[19] E. Polizzi and S. Datta, IEEE Trans. Nanotechnol. **2003**, 40 (2003).
[20] P. Havu, V. Havu, M. J. Puska, and R. M. Nieminen, Phys. Rev. B **69**, 115325 (2004).
[21] R. Buczko, S. J. Pennycook, and S. T. Pantelides, Phys. Rev. Lett. **84**, 943 (2000).
[22] R. Landauer, IBM J. Res. Dev. **1**, 233 (1957).
[23] R. Landauer, Philos. Mag. **21**, 863 (1970).
[24] Y. Imry, *Introduction to Mesoscopic Physics* (Oxford University Press, New York, 2002).
[25] L. P. Kadanoff and G. Baym, *Quantum Statistical Mechanics* (Benjamin, New York, 1962).
[26] P. Havu, V. Havu, M. J. Puska, M. H. Hakala, A. S. Foster, and R. M. Nieminen, J. Chem. Phys. **124**, 054707 (2006).
[27] P. O. Persson and G. Strang, SIAM Rev. **46**, 329 (2004).
[28] S. M. Goodnick, D. K. Ferry, C. W. Wilmsen, Z. Liliental, D. Fathy, and O. L. Krivanek, Phys. Rev. B **32**, 8171 (1985).
[29] W. D. Sheng, J. Phys.: Condens. Matter **9**, 8369 (1997).
[30] International Technology Roadmap for Semiconductors, 2007, http://www.itrs.net/
[31] R. de L. Kronig and W. G. Penny, Proc. R. Soc. London, Ser. A **130**, 499 (1931).
[32] K. Uchida, J. Koga, and S. I. Takagi, Tech. Dig. - Int. Electron Devices Meet. **2003**, 805.
[33] F. Stern and W. E. Howard, Phys. Rev. **163**, 816 (1967).
[34] T. Low, M. F. Li, G. Samudra, Y. C. Yeo, C. Zhu, and D. L. Kwong, IEEE Trans. Electron Devices **52**, 2430 (2005).